

ROBUST FAULT DIAGNOSIS FOR AERO-ENGINE NETWORKED CONTROL SYSTEMS UNDER TRANSMISSION UNCERTAINTIES

LinJun Lu[1], YuZhi Chen[1,*], GuangAo Liang[1] & LinFeng Gou[1]

[1]School of Power and Energy, Northwestern Polytechnical University, Xi'an, China

Abstract

Networked and distributed control is becoming a key enabling architecture for modern aero-engines, playing a crucial role in full-envelope safety, mission reliability, thrust–attitude coordination, and online health management. However, transmission uncertainties inherent in communication networks, such as time delays, packet dropouts, and link jitter, can disrupt the temporal consistency between measurements and control commands. These effects may further induce non-Gaussian and time-varying equivalent noise, for which conventional estimation- and residual-based fault diagnosis methods are limited. To address this problem, this study proposes a robust fault diagnosis methodology for a networked distributed control system of a high-bypass-ratio turbofan engine under severe transmission uncertainties. The propagation mechanisms of sensor faults, actuator faults, and network-induced anomalies are first analysed in the closed-loop system, and a unified fault propagation model is established to derive an augmented fault-space representation. Based on this representation, an unscented Kalman filter incorporating an adaptive kernel-bandwidth minimum information entropy criterion is developed to improve robustness against non-Gaussian and time-varying disturbances. A full-dimensional fault detector is then constructed for system-level fault detection. To satisfy node-level diagnostic requirements, a fault collapse coefficient is embedded into a bank of reduced-order filters to attenuate fault coupling from other nodes, thereby enabling simultaneous node-level fault isolation and fault severity estimation. Simulation results demonstrate that the proposed method maintains a fault detection rate above 98%, a node-level fault isolation rate exceeding 99%, and a fault estimation accuracy of approximately 99.4%–99.8%, even when the packet loss rate reaches 75%. These results suggest that the proposed framework can improve robust fault diagnosis for aero-engine networked control systems under severe packet-loss conditions.

Keywords: Aero-engine, Networked Control System, Fault Diagnosis, Fault Propagation Model

1. Introduction

The reliability of aero-engine control systems is directly associated with flight safety, mission continuity, and stable propulsion-system operation over the full flight envelope [1]. For modern high-bypass-ratio turbofan engines, the control system increasingly integrates sensing, actuation, communication, onboard computation, fault diagnosis, and health-management functions into a safety-critical cyber-physical system [2]. Recent studies on gas-turbine and aero-engine health management have highlighted the importance of uncertainty representation, health degradation estimation, digital-twin modelling, and real-time gas-path fault diagnosis for improving engine safety and operational reliability [3–6]. These developments indicate that next-generation aero-engine control systems require diagnostic methods that can operate reliably not only under complex thermodynamic dynamics but also under communication-induced uncertainties introduced by distributed control architectures.

Driven by the demand for lighter, more modular, and more intelligent propulsion control systems, aero-engine control architectures are gradually shifting from conventional centralized full-authority digital electronic control systems to networked and distributed configurations [7]. In a distributed

https://doi.org/10.71945/icas2026_0149

architecture, sensing, computation, and actuation functions can be assigned to intelligent nodes connected by communication links, thereby reducing wiring complexity, alleviating the computational burden of the central controller, and providing an architectural basis for node-level fault isolation and local fault tolerance [8,9]. However, the communication network also becomes a part of the closed-loop system. Transmission delays, packet dropouts, link jitter, scheduling mechanisms, and node heterogeneity may alter the effective arrival time and validity of sensor measurements and actuator commands. As a result, network-induced anomalies may enter both the input and output channels and become coupled with physical sensor and actuator faults in the residual space. This coupling poses a significant challenge to aero-engine fault diagnosis [10].

Conventional centralized diagnostic methods usually assume that measurement information and control commands are temporally consistent, and that process and measurement noise can be approximated by Gaussian distributions. Under networked distributed control, these assumptions may be violated. Packet losses can force nodes to use held, predicted, or fail-safe values; transmission delays can break the synchronization between controller states and sensor outputs; and link jitter can introduce irregular residual fluctuations. Research on networked systems has shown that packet dropouts, time-varying delays, and communication constraints can substantially affect state estimation, residual generation, and fault decision logic [11,12]. Nevertheless, most of these studies are formulated for general nonlinear or stochastic networked systems, whereas aero-engine distributed control systems further involve strong nonlinear thermodynamic dynamics, multi-variable coupling, and strict real-time safety constraints.

Existing aero-engine fault diagnosis studies have made substantial progress in model-based filtering, uncertainty-aware health estimation, digital-twin diagnosis, and deep-learning-based fault recognition [13–16]. These methods demonstrate the potential of combining physical modelling and data-driven learning in engine health management. However, several limitations remain when they are applied to networked distributed engine control. First, sensor faults, actuator faults, and network-induced anomalies are often treated separately, and a unified fault-space representation for aero-engine networked distributed control systems remains insufficiently developed. Second, residual-based detection methods relying on Gaussian assumptions may suffer from biased estimation and threshold mismatch when packet dropouts and delays generate non-Gaussian, time-varying, or heavy-tailed equivalent noise. Although entropy-based robust Kalman filters have shown advantages in dealing with non-Gaussian disturbances [17–20], their application to aero-engine networked fault diagnosis remains limited. Third, distributed architectures introduce inter-node fault coupling, making it difficult to determine whether a residual abnormality originates from the node under diagnosis, from another coupled node, or from the communication network itself.

Therefore, a research gap remains in developing a unified and robust diagnostic framework that can simultaneously represent physical component faults and network-induced anomalies, generate reliable residuals under non-Gaussian transmission uncertainty, and isolate node-level faults in the presence of inter-node coupling.

To address these problems, this paper proposes a robust fault diagnosis methodology for a networked distributed control system of a high-bypass-ratio turbofan engine under transmission uncertainties. Unlike previous studies that treat physical faults and communication anomalies separately, this study formulates both effects within a unified augmented fault-space representation. On this basis, an adaptive kernel-bandwidth minimum-information-entropy UKF is developed for robust residual generation under non-Gaussian and time-varying disturbances. A full-dimensional detector is constructed for system-level fault detection, while a bank of reduced-order filters with a fault collapse coefficient is designed for node-level fault isolation and fault severity estimation.

The principal contributions of this paper are summarised as follows:

1. A unified fault propagation model is established for aero-engine networked control systems, enabling sensor faults, actuator faults, and network-induced anomalies to be described in an

equivalent augmented fault space.

2. An adaptive kernel-bandwidth minimum-information-entropy UKF is proposed to enhance the robustness of residual generation under non-Gaussian and time-varying disturbances caused by transmission uncertainty.
3. A reduced-order node-level diagnostic structure with a fault collapse coefficient is developed to attenuate inter-node fault coupling and realise simultaneous fault isolation and fault severity estimation.

The remainder of this paper is organised as follows. Section 2 describes the control system augmented fault propagation model, and the proposed robust filtering and node-level diagnosis algorithms. Section 3 presents the simulation setup and evaluates the diagnostic performance under different packet-loss conditions. Section 4 discusses the robustness, limitations, and engineering implications of the proposed method.

2. Methodology

2.1 Networked Control System Architecture

The investigated plant is a high-bypass-ratio turbofan engine equipped with a distributed networked control system. In contrast to a conventional centralized FADEC architecture, the proposed architecture decomposes sensing, control computation, actuation and diagnostic functions into several time-triggered nodes. These nodes exchange measurement data, control commands and health-management information through redundant communication buses. The resulting structure is intended to reduce wiring complexity and computational concentration while preserving deterministic timing, which is essential for aero-engine control applications.

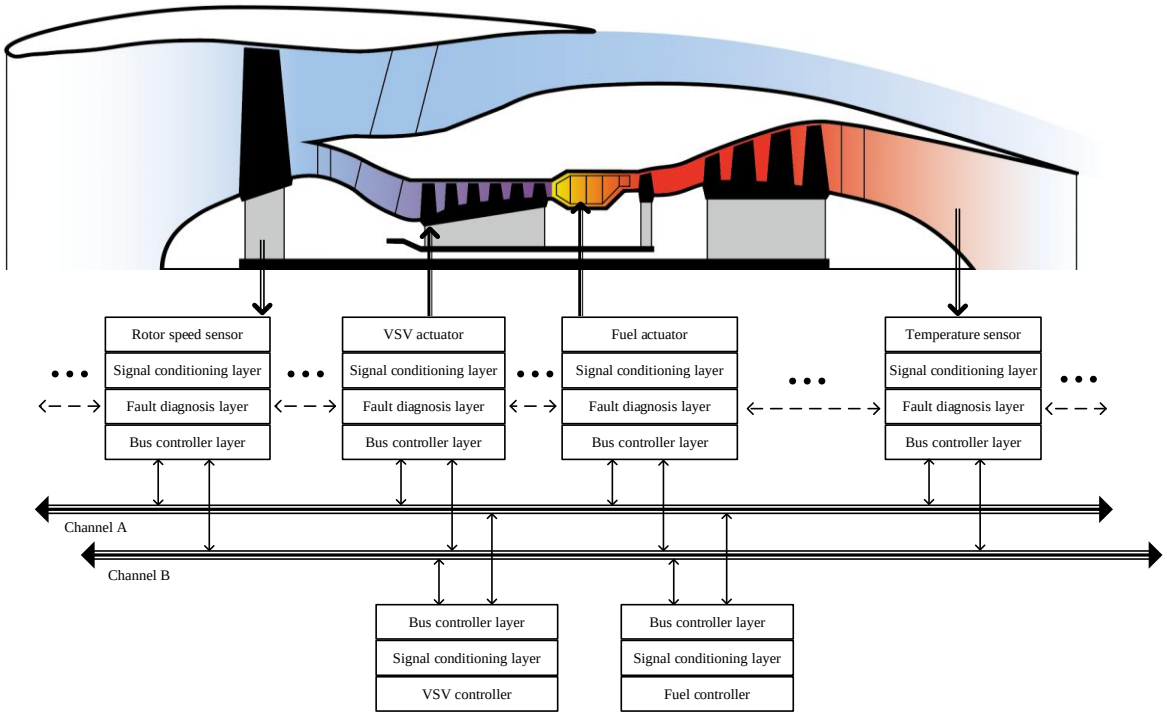


Figure 1 – Networked control system architecture for a turbofan engine

The communication layer is designed around a time-triggered protocol, in which all nodes share a global time base and transmit frames according to an offline static schedule. Sensor nodes acquire and preprocess key engine variables. Actuator nodes execute control commands. Controller nodes receive the scheduled measurements, evaluate the control law and logic constraints, and send commands to the corresponding actuator nodes. Because the node functions and the data-frame sequence are specified at the design stage, the architecture avoids dynamic bus competition and

reduces timing uncertainty in the closed loop.

A separate diagnostic bus is reserved for health-state information, node monitoring data and fault-diagnosis messages. This separation decouples health-management traffic from the main control data stream, so that diagnostic communication does not interfere with the control loop. It also provides a structural basis for later system-level detection, node-level isolation and fault-tolerant control.

Each intelligent node is organised as four functional layers: a sensor/actuator acquisition layer, a signal conditioning layer, a fault-diagnosis layer and a bus-controller layer. The acquisition layer interfaces with local sensors or actuators. The conditioning layer performs nonlinear correction, range scaling and signal preprocessing. The diagnostic layer compares locally processed information with bus-transmitted control signals to support node-side fault evaluation. The bus-controller layer parses and transmits time-triggered frames. Although these layers are functionally independent, they operate under the same clock and therefore maintain a clear sequence of acquisition, conditioning, diagnosis and communication.

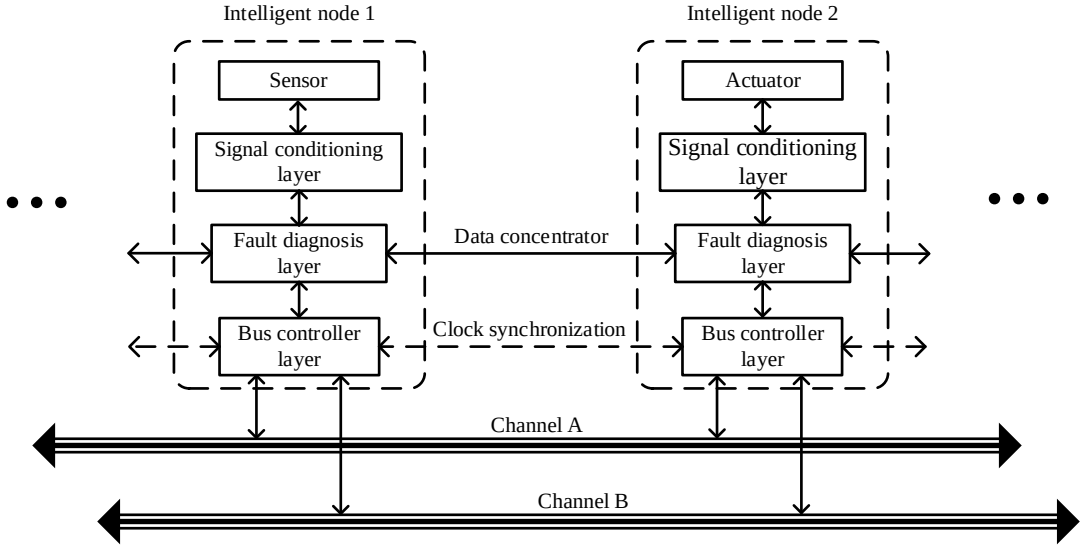


Figure 2 – Intelligent node architecture based on the time-triggered bus

The controller node follows the same modular principle. Its core modules include control-logic computation, internal signal interfacing and bus communication. After receiving the scheduled sensor and node-state information, the controller performs local control-law calculation and then sends the resulting commands through the time-triggered bus. If one controller node degrades or fails, the effect can be confined to a local control function rather than immediately propagating to the whole engine control system. This architectural localisation is an important prerequisite for node-level fault isolation.

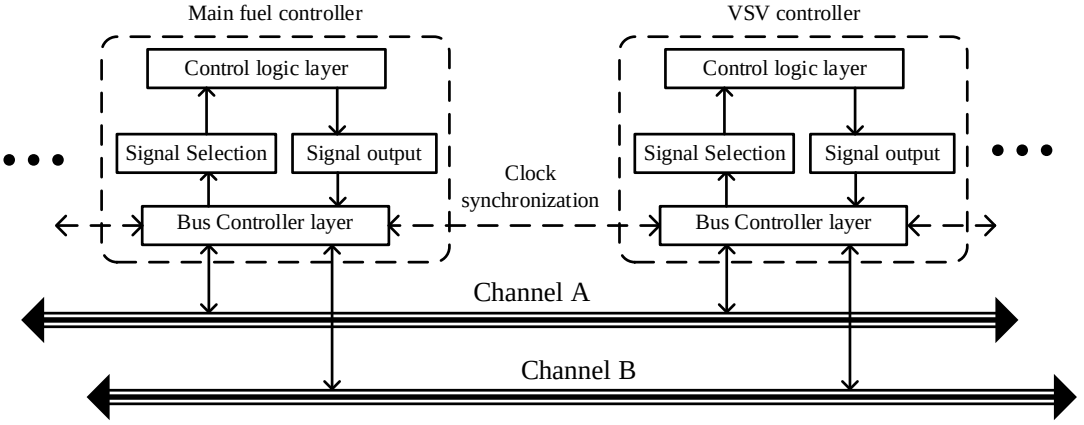


Figure 3 – Controller node architecture based on the time-triggered bus

In one 15 ms control period, the sensor node first samples the engine state and transmits it to the fuel controller; the fuel command is then sent to the fuel actuator; after the fuel-loop execution is completed, the VSV controller and VSV actuator are scheduled in sequence. This sample-control-execute timing chain is used as the basis for subsequent fault-propagation and diagnosis modelling. The network configuration of the established networked control system is listed in the following table.

Table 1 – Communication network parameters and static scheduling configuration

Parameter name	Parameter value	Description
Network type	TDMA	Time-division multiple access is adopted
Network number	1	Communication network instance number
Number of nodes	5	Total number of nodes participating in communication
Data rate	320kbps	Data transmission rate at the physical layer
Minimum frame size	160bit	Minimum bit length of a single communication frame
Slot size	160bit	Bit length corresponding to a single time slot
Loss probability	0	Random packet loss probability
Initial seed	0	Network random seed
Static schedule	[5 1 3 2 4]	Data transmission order of each node

The scheduling timing logic of each node is shown in the following figure.

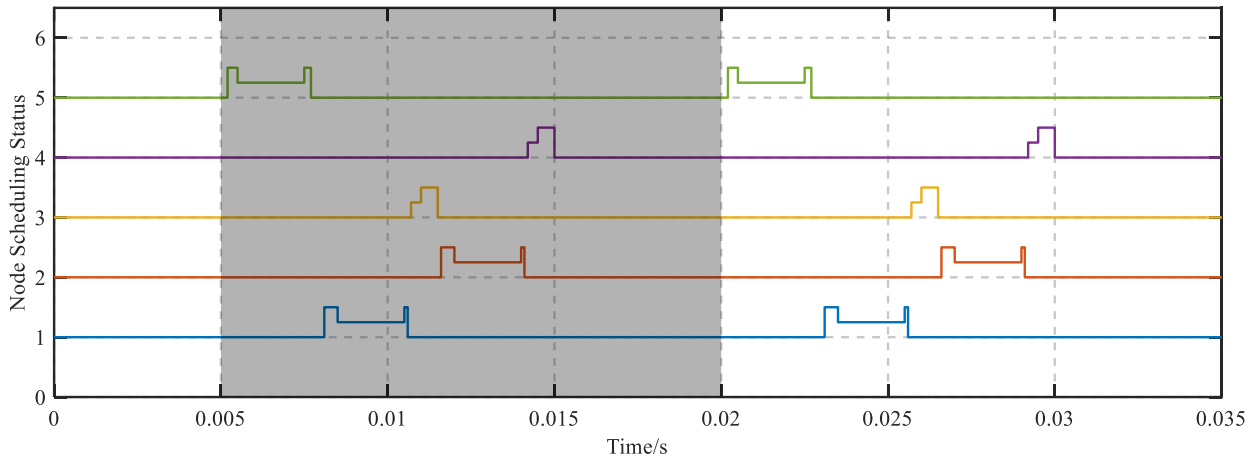


Figure 4 – Network scheduling sequence of all nodes within one control period

2.2 Networked Control System Fault Propagation Model

The diagnostic model is formulated by treating physical component faults and network-induced anomalies in a unified fault space. A fault is interpreted as an additional deviation that causes the actual system response to depart from its nominal response. This representation is sufficiently general to describe structural degradation, parameter drift, bias faults and information distortion, because each of these phenomena ultimately introduces an additive or equivalent additive component in the measured or controlled variable.

$$\boldsymbol{z}_{Act} = \boldsymbol{z}_{Normal} + \Delta \boldsymbol{z} \tag{1}$$

For a nonlinear aero-engine control system, actuator faults and sensor faults have different propagation characteristics. An actuator fault enters through the input channel and therefore affects both the current output and the future state trajectory. A sensor fault acts directly on the output measurement and may propagate further only when the corrupted measurement is fed back into the controller. After local linearisation and discretisation around an operating point, the open-loop fault model can be written in state-space form with separate input-side and output-side fault terms.

$$\begin{aligned}\Delta \boldsymbol{x}(k+1) &= \boldsymbol{A}\Delta \boldsymbol{x}(k) + \boldsymbol{B}(\Delta \boldsymbol{u}(k) + \boldsymbol{f}_A(k)) \\ \Delta \boldsymbol{y}(k) &= \boldsymbol{C}\Delta \boldsymbol{x}(k) + \boldsymbol{D}(\Delta \boldsymbol{u}(k) + \boldsymbol{f}_A(k)) + \boldsymbol{f}_S(k)\end{aligned} \tag{2}$$

In a networked control system, communication uncertainty can be represented in the same modelling framework. Input-side delay means that the actuator receives an outdated command rather than the current controller output; output-side delay means that the controller receives outdated measurement information. The difference between the delayed signal and the nominal current signal is therefore equivalent to an additional network-induced input or output fault.

$$\begin{cases}\boldsymbol{\delta}_u(k) = \Delta \boldsymbol{u}(k - \tau_u(k)) - \Delta \boldsymbol{u}(k) \\ \boldsymbol{\delta}_y(k) = \Delta \boldsymbol{y}(k - \tau_y(k)) - \Delta \boldsymbol{y}(k)\end{cases} \tag{3}$$

Packet dropout is handled similarly by introducing a binary random reachability variable, which indicates whether a control or measurement frame is successfully received at the current sampling instant. If the frame is lost, the node uses a held or unavailable signal, producing an equivalent deviation from the nominal transmission.

$$\begin{cases}\Delta \boldsymbol{u}_{Act}(k) = \Gamma_u(k)\Delta \boldsymbol{u}(k - \tau_u(k)) \\ \Delta \boldsymbol{y}_{Act}(k) = \Gamma_y(k)\Delta \boldsymbol{y}(k - \tau_y(k))\end{cases} \tag{4}$$

Consequently, faults in the control system and the communication network can be described by the following complex fault-propagation architecture.

$$\begin{aligned}\Delta \boldsymbol{x}(k+1) = {} & \boldsymbol{A}\Delta \boldsymbol{x}(k) + \boldsymbol{B}\Delta \boldsymbol{u}(k) + \boldsymbol{B}(\Gamma_u(k)\Delta \boldsymbol{u}(k - \tau_u(k)) - \Delta \boldsymbol{u}(k)) \\ & + \boldsymbol{B}\boldsymbol{f}_A(k) \\ \Delta \boldsymbol{y}(k) = {} & \boldsymbol{C}\Delta \boldsymbol{x}(k) + \boldsymbol{D}\Delta \boldsymbol{u}(k) + \boldsymbol{D}(\Gamma_u(k)\Delta \boldsymbol{u}(k - \tau_u(k)) - \Delta \boldsymbol{u}(k)) \\ & + \boldsymbol{D}\boldsymbol{f}_A(k) + \boldsymbol{f}_S(k) \\ & + \Gamma_y(k)\boldsymbol{\delta}_y(k) + (\Gamma_y(k) - 1)\boldsymbol{\xi}(k)\end{aligned} \tag{5}$$

Where $\boldsymbol{\xi}(k) = (\boldsymbol{C}\Delta \boldsymbol{x}(k) + \boldsymbol{D}\Delta \boldsymbol{u}(k) + \boldsymbol{D}(\Gamma_u(k)\Delta \boldsymbol{u}(k - \tau_u(k)) - \Delta \boldsymbol{u}(k)) + \boldsymbol{D}\boldsymbol{f}_A(k) + \boldsymbol{f}_S(k))$.

Network delay, packet loss, actuator faults and sensor faults can be merged into an augmented fault vector.

$$\begin{cases}\boldsymbol{f}_u(k) = \Gamma_u(k)\Delta \boldsymbol{u}(k - \tau_u(k)) - \Delta \boldsymbol{u}(k) \\ \boldsymbol{f}_y(k) = \Gamma_y(k)\boldsymbol{\delta}_y(k) + (\Gamma_y(k) - 1)\boldsymbol{\xi}(k)\end{cases} \tag{6}$$

In this augmented representation, the conventional control-system fault space and the network fault space share the same input-output structure.

$$\begin{aligned}\Delta \boldsymbol{x}(k+1) &= \boldsymbol{A}\Delta \boldsymbol{x}(k) + \boldsymbol{B}\Delta \boldsymbol{u}(k) + \begin{pmatrix}\boldsymbol{B} & \boldsymbol{0}\end{pmatrix}\begin{pmatrix}\boldsymbol{f}_u(k) & \boldsymbol{f}_y(k)\end{pmatrix}^T + \begin{pmatrix}\boldsymbol{B} & \boldsymbol{0}\end{pmatrix}\begin{pmatrix}\boldsymbol{f}_A(k) & \boldsymbol{f}_S(k)\end{pmatrix}^T \\ \Delta \boldsymbol{y}(k) &= \boldsymbol{C}\Delta \boldsymbol{x}(k) + \boldsymbol{D}\Delta \boldsymbol{u}(k) + \begin{pmatrix}\boldsymbol{D} & \boldsymbol{I}\end{pmatrix}\begin{pmatrix}\boldsymbol{f}_u(k) & \boldsymbol{f}_y(k)\end{pmatrix}^T + \begin{pmatrix}\boldsymbol{D} & \boldsymbol{I}\end{pmatrix}\begin{pmatrix}\boldsymbol{f}_A(k) & \boldsymbol{f}_S(k)\end{pmatrix}^T\end{aligned} \tag{7}$$

Where $\begin{pmatrix}\boldsymbol{f}_A(k) & \boldsymbol{f}_S(k)\end{pmatrix}^T$ is described control-system fault space, $\begin{pmatrix}\boldsymbol{f}_u(k) & \boldsymbol{f}_y(k)\end{pmatrix}^T$ is described network fault space.

Finally, the fault propagation model of networked control system as follows:

$$\begin{aligned}\Delta \boldsymbol{x}(k+1) &= \boldsymbol{A}\Delta \boldsymbol{x}(k) + \boldsymbol{B}\Delta \boldsymbol{u}(k) + \begin{pmatrix}\boldsymbol{B} & \boldsymbol{0}\end{pmatrix}\begin{pmatrix}\boldsymbol{f}_A(k) & \boldsymbol{f}_S(k)\end{pmatrix}^T + \bar{\boldsymbol{\omega}}(k) \\ \Delta \boldsymbol{y}(k) &= \boldsymbol{C}\Delta \boldsymbol{x}(k) + \boldsymbol{D}\Delta \boldsymbol{u}(k) + \begin{pmatrix}\boldsymbol{D} & \boldsymbol{I}\end{pmatrix}\begin{pmatrix}\boldsymbol{f}_A(k) & \boldsymbol{f}_S(k)\end{pmatrix}^T + \bar{\boldsymbol{v}}(k)\end{aligned} \tag{8}$$

where $\bar{\boldsymbol{\omega}}(k)$ and $\bar{\boldsymbol{v}}(k)$ denote composite noises induced by network transmission, each formed by the superposition of non-Gaussian and Gaussian noise components; therefore, neither follows a

Gaussian distribution.

The principal difference is statistical: the equivalent noise caused by network transmission combines Gaussian measurement uncertainty with non-Gaussian disturbance components introduced by delay and dropout. This non-Gaussian characteristic motivates the use of the adaptive minimum-information-entropy unscented Kalman filter in the residual-generation stage.

2.3 Adaptive Minimum Information Entropy Criterion Unscented Kalman Filter

Network time delay packet loss, and other transmission uncertainties do not follow a conventional Gaussian distribution, filter structures designed under the assumption of Gaussian noise cannot effectively suppress non-Gaussian noise. Therefore, study uses the adaptive minimum-information-entropy criterion within the UKF framework to improve the robustness of the filter under non-Gaussian noise.

The minimum-information-entropy criterion evaluates the uncertainty of the filtering error distribution.

$$J = -\log_2\left(\sum_{i=1}^{n} P(e_i)^2\right) \tag{9}$$

Where $P(x)$ is the probability of the event x occurring.

A Gaussian kernel is used to estimate the residual distribution through a Parzen-window approximation.

$$\hat{J} = \frac{\bar{N}^2}{\sum_{i=1}^{\bar{N}}\sum_{j=1}^{\bar{N}} k_\sigma(e_i(k) - e_j(k))} \tag{10}$$

Where $\bar{N}$ is the width of window, σ is the bandwidth of gaussian kernel function.

And the kernel bandwidth is adjusted according to the predicted allowable error and the current estimation condition.

$$\sigma(k) = \| \boldsymbol{y}_{Predict}(k) - \hat{\boldsymbol{y}}(k \mid k-1) \|_{\boldsymbol{R}^{-1}(k)} \tag{11}$$

Where $\boldsymbol{y}_{Predict}$ is the allowable error output calculated by system, $\hat{\boldsymbol{y}}$ is the estimate output from filter, $\| \boldsymbol{x} \|_A$ is defined $(\boldsymbol{x}^T \boldsymbol{A} \boldsymbol{x})^{1/2}$, and $\boldsymbol{R}(k)$ is covariance matrix of measurement equation.

Based on the above method, the filter gain calculation of the AMinIEC-UKF is transformed into solving for the minimum of the cost function J:

$$\begin{aligned} J(k) = & \underbrace{k_\sigma(\| \boldsymbol{x}(k) - \hat{\boldsymbol{x}}(k \mid k-1) \|_{\boldsymbol{P}^{-1}(k|k-1)})}_{J_1(k)} + \\ & \underbrace{k_\sigma(\| \boldsymbol{y}(k) - \hat{\boldsymbol{y}}(k \mid k-1) - \boldsymbol{H}(k)(\boldsymbol{x}(k) - \hat{\boldsymbol{x}}(k \mid k-1)) \|_{\bar{\boldsymbol{R}}^{-1}(k)})}_{J_2(k)} \end{aligned} \tag{12}$$

Where $\boldsymbol{H}(k)$ is the measurement equation.

Finally, the filter gain is given by:

$$\bar{\boldsymbol{K}}(k) = (\boldsymbol{P}^{-1}(k \mid k-1) + \zeta \boldsymbol{H}(k))^{-1} \zeta \tag{13}$$

Where ζ is defined $k_\sigma(\| \boldsymbol{y}(k) - \hat{\boldsymbol{y}}(k \mid k-1) \|^2_{\bar{\boldsymbol{R}}^{-1}(k)}) \boldsymbol{H}(k)^T \bar{\boldsymbol{R}}^{-1}(k)$.

In this way, abnormal residual samples caused by non-Gaussian disturbances are suppressed without discarding useful state information.

2.4 Networked Control System Fault Detection Isolation and Accommodation

As shown in the figure 5, the complete diagnostic structure contains two coordinated modules: a full-

order filter for system-level detection and a reduced-order filter bank for node-level isolation and estimation. The full-order filter answers whether the networked control system is abnormal, while the reduced-order filters identify where the abnormality is most likely located and estimate its severity. This division is suitable for a distributed FADEC architecture because it separates global health monitoring from local node diagnosis. It also limits fault coupling: once a node-level model excludes the suspected faulty information path, the remaining model can estimate the engine state and the fault magnitude with reduced contamination from neighbouring nodes.

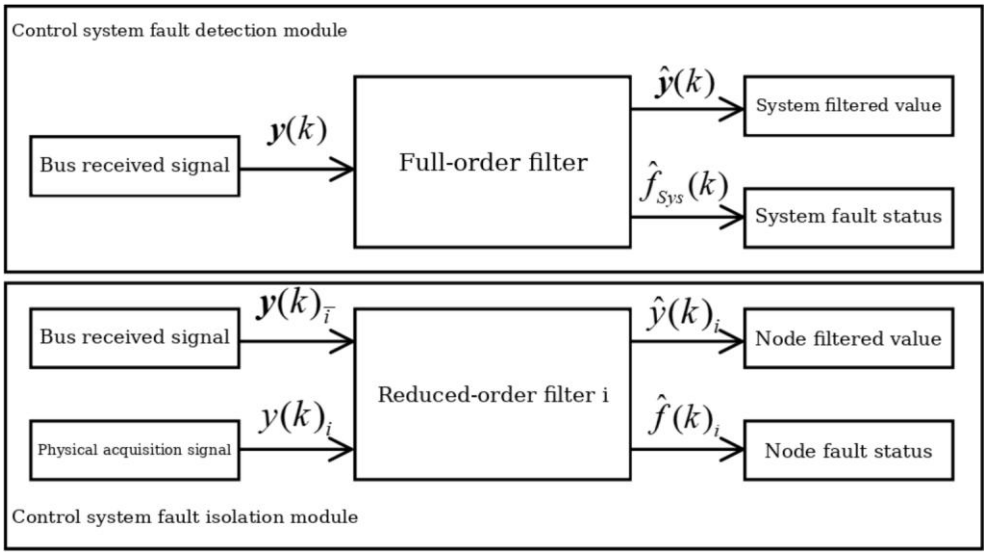


Figure 5 – Architecture of network control system fault detection isolation and accommodation

System-level fault detection is performed by a full-order robust filtering module. The full-order filter uses all available measurement channels to estimate the engine state and to generate a prediction of the measured outputs.

According to Eq. (8), it can be rewritten as the following state-space model:

$$\begin{aligned}\begin{pmatrix}\Delta\boldsymbol{x}(k+1)\\ \boldsymbol{f}_A(k+1)\\ \boldsymbol{f}_S(k+1)\end{pmatrix}&=\left(\begin{array}{c|c}\boldsymbol{A} & \boldsymbol{B}_A \mid \boldsymbol{0}\\ \hline & diag(\boldsymbol{K}_A,\boldsymbol{K}_S)\end{array}\right)\begin{pmatrix}\Delta\boldsymbol{x}(k)\\ \boldsymbol{f}_A(k)\\ \boldsymbol{f}_S(k)\end{pmatrix}+\boldsymbol{B}\Delta\boldsymbol{u}(k)+\begin{pmatrix}\bar{\boldsymbol{\omega}}(k)\\ \\ \end{pmatrix}\\ \Delta\boldsymbol{y}(k)&=\begin{pmatrix}\boldsymbol{C} & \boldsymbol{D}_A \mid \boldsymbol{I}\end{pmatrix}\begin{pmatrix}\Delta\boldsymbol{x}(k)\\ \boldsymbol{f}_A(k)\\ \boldsymbol{f}_S(k)\end{pmatrix}+\boldsymbol{D}\Delta\boldsymbol{u}(k)+\bar{\boldsymbol{v}}(k)\end{aligned} \tag{14}$$

where $\boldsymbol{B}_A$ is the subset of the $\boldsymbol{B}$ matrix corresponding to the actuator input channel, $\boldsymbol{D}_A$ is the subset of the $\boldsymbol{D}$ matrix corresponding to the actuator input channel, and $\boldsymbol{K}_A$ and $\boldsymbol{K}_S$ are the node fault gain vectors. If node i is a sensor node, then $\boldsymbol{K}_A=0$, and the element of $\boldsymbol{K}_S$ corresponding to the i-th row and i-th column is λ, while all the remaining elements are zero. Here, λ is the node fault collapse coefficient, with $\lambda\in[0,1]$.

Therefore, for a single node, the fault model at the node is reduced to the following form:

$$\begin{aligned}\begin{pmatrix}\Delta\boldsymbol{x}(k+1)\\ \hat{f}(k+1)_i\end{pmatrix}&=\left(\begin{array}{c|c}\boldsymbol{A} & (\boldsymbol{B}_A \mid \boldsymbol{0})_{(:,i)}\\ \hline & \lambda\boldsymbol{e}_i\boldsymbol{e}_i^T\end{array}\right)\begin{pmatrix}\Delta\boldsymbol{x}(k)\\ \hat{f}(k)_i\end{pmatrix}+\boldsymbol{B}\Delta\boldsymbol{u}(k)+\begin{pmatrix}\bar{\boldsymbol{\omega}}(k)\\ \\ \end{pmatrix}\\ \Delta\boldsymbol{y}(k)&=\begin{pmatrix}\boldsymbol{C} & (\boldsymbol{D}_A \mid \boldsymbol{I})_{(:,i)}\end{pmatrix}\begin{pmatrix}\Delta\boldsymbol{x}(k)\\ \hat{f}(k)_i\end{pmatrix}+\boldsymbol{D}\Delta\boldsymbol{u}(k)+\bar{\boldsymbol{v}}(k)\end{aligned} \tag{15}$$

where $\boldsymbol{e}_i$ is a unit column vector, and $(\boldsymbol{A})_{(:,i)}$ denotes all elements in the i-th column of matrix $\boldsymbol{A}$.

The system shown in Eq. (14) is the fault detection model for the distributed control system, while the structure shown in Eq. (15) is the node fault isolation and accommodation model for the networked control system.

The residual is defined as the difference between the actual measurement and the filter-predicted output. A weighted sum of squared residuals (WSSR) is then calculated as the fault-evaluation statistic.

$$\begin{aligned} \Delta \boldsymbol{y}(k) &= \boldsymbol{y}(k) - \hat{\boldsymbol{y}}(k) \\ WSSR(k) &= \Delta \boldsymbol{y}(k)^T \boldsymbol{\Theta}(k) \Delta \boldsymbol{y}(k) \end{aligned} \tag{16}$$

Where, $\boldsymbol{\Theta}(k)$ is the residual weighting matrix.

Under normal operation, the residual remains close to the uncertainty range of the measurement system; when a sensor, actuator or network-induced equivalent fault occurs, the residual increases and the WSSR crosses the detection threshold.

Once the system-level module indicates an abnormal condition, node-level isolation and fault accommodation are carried out by a reduced-order filter bank. The method follows the principle that a filter excluding the faulty measurement channel can still provide a reliable state estimate, whereas a filter that includes the faulty channel will inherit the fault information and produce an increased residual statistic.

By comparing the WSSR values of multiple reduced-order filters constructed from different measurement subsets, the faulty node can be isolated. The same predicted output can also be used to reconstruct the corrupted measurement, which provides corrected information for subsequent fault-tolerant control.

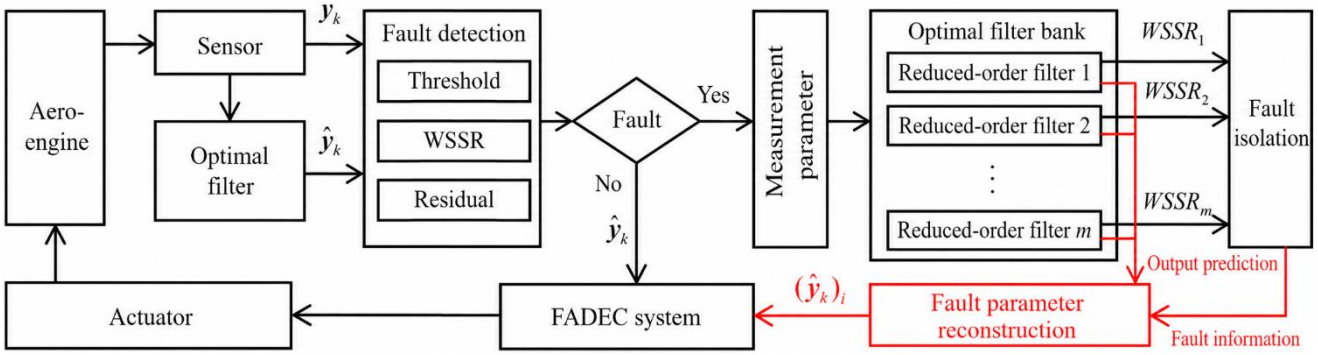


Figure 6 – Typical fault-diagnosis system based on a reduced-order optimal filter

The estimated node fault is obtained by applying the AMinIEC-UKF to the fault model. The resulting node-level output consists of the isolated node label, the estimated fault coefficient and the reconstructed measurement or command where applicable. These outputs provide the information required by a higher-level accommodation or reconfiguration strategy, although the present paper focuses on diagnosis rather than closed-loop fault-tolerant control.

3. Results

3.1 Simulation Setup

The experimental validation is conducted under both steady-state and dynamic operating conditions. The fault injection strategy is kept identical in the two experiments, while the engine operating state is changed to evaluate the fault diagnosis performance under different conditions.

Case 1: Steady-state experiment, the cruise operating condition of the engine at $H = 11km$, $Ma = 0.85$, and $PcnL = 100\%$ is selected as the test condition. The simulation time is set to 550s.

Starting from $t=10s$, 11 different faults are injected sequentially with a slope of $-0.01/\mathrm{s}$, decreasing from 1.00 to 0.95. Each fault is then held for 25s and subsequently removed with a slope of $0.01/\mathrm{s}$. The specific fault injection sequence is shown in Figure 7.

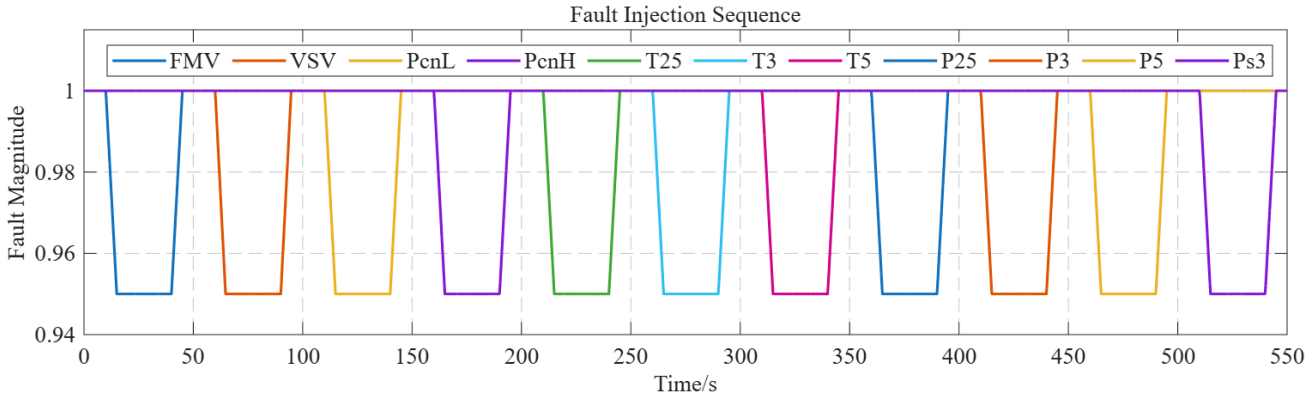


Figure 7 – Sequential fault injection profile

Case 2: Dynamic-state experiment, the same cruise operating condition is used as the initial operating point. The simulation time is also set to 550s. During the simulation, a controller is adopted to regulate the $PcnL$. From $t=5s$, the $PcnL$ decreases continuously at a slope of $-5\ \mathrm{rpm/s}$ until the end of the simulation. Starting from $t=10s$, the same 11 faults are injected sequentially.

To evaluate the influence of distributed-bus packet loss on fault diagnosis under both steady-state and dynamic conditions, four packet-loss cases are considered. The packet loss rates of the distributed bus are set to 0%, 25%, 50%, and 75%, respectively.

Evaluation metrics include fault detection rate, false alarm rate, node fault isolation rate, and fault estimation accuracy. The fault detection rate measures the ability to identify true fault states; the false alarm rate characterizes the probability of a fault-free state being misclassified as faulty; the node fault isolation rate and fault estimation accuracy evaluate the fault localization capability and the fault severity reconstruction capability, respectively.

3.2 Fault Detection Results

Under closed-loop control conditions, the steady-state case is shown in the figure 8. Since this study focuses on fault diagnosis of the control system rather than fault-tolerant control, the reconstructed signal values obtained from the fault diagnosis results are not fed back to the control system in real time to assist closed-loop control. This arrangement is intended to demonstrate the effectiveness of the proposed fault diagnosis method and to avoid the influence of controller robustness on the diagnostic results.

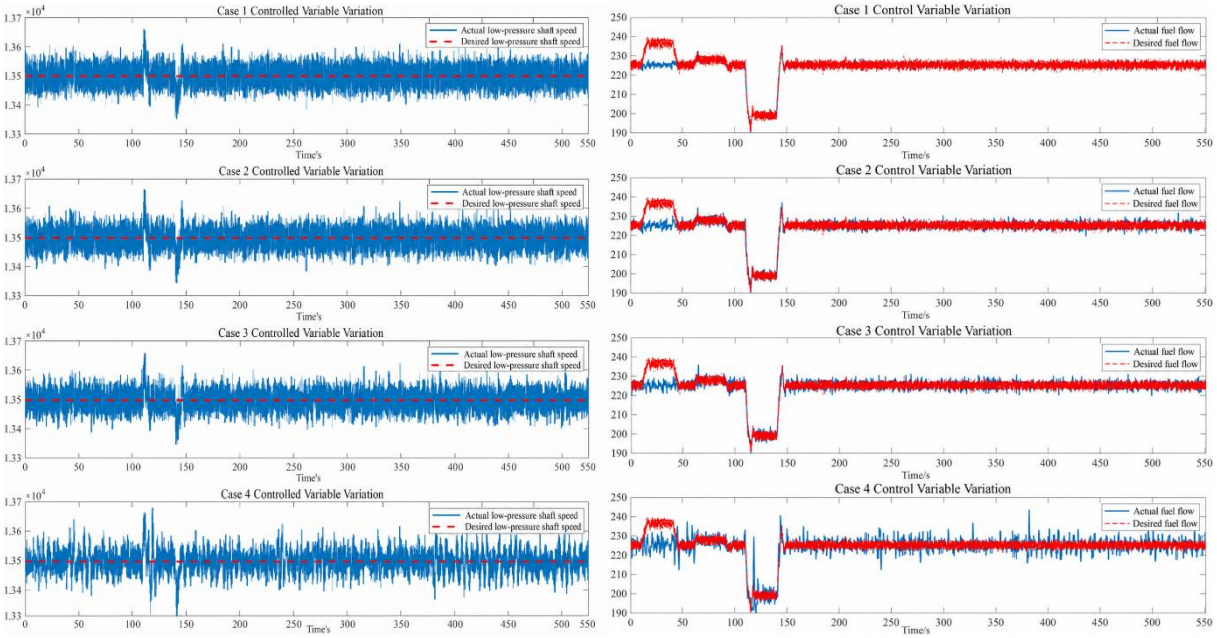


Figure 8 – Variations in controlled variable and control variable under steady-state condition

Communication packet loss alters the fluctuation characteristics of both control and controlled variables, the AMinIEC-UKF full-dimensional fault detector maintains a high fault detection rate under all packet loss conditions examined.

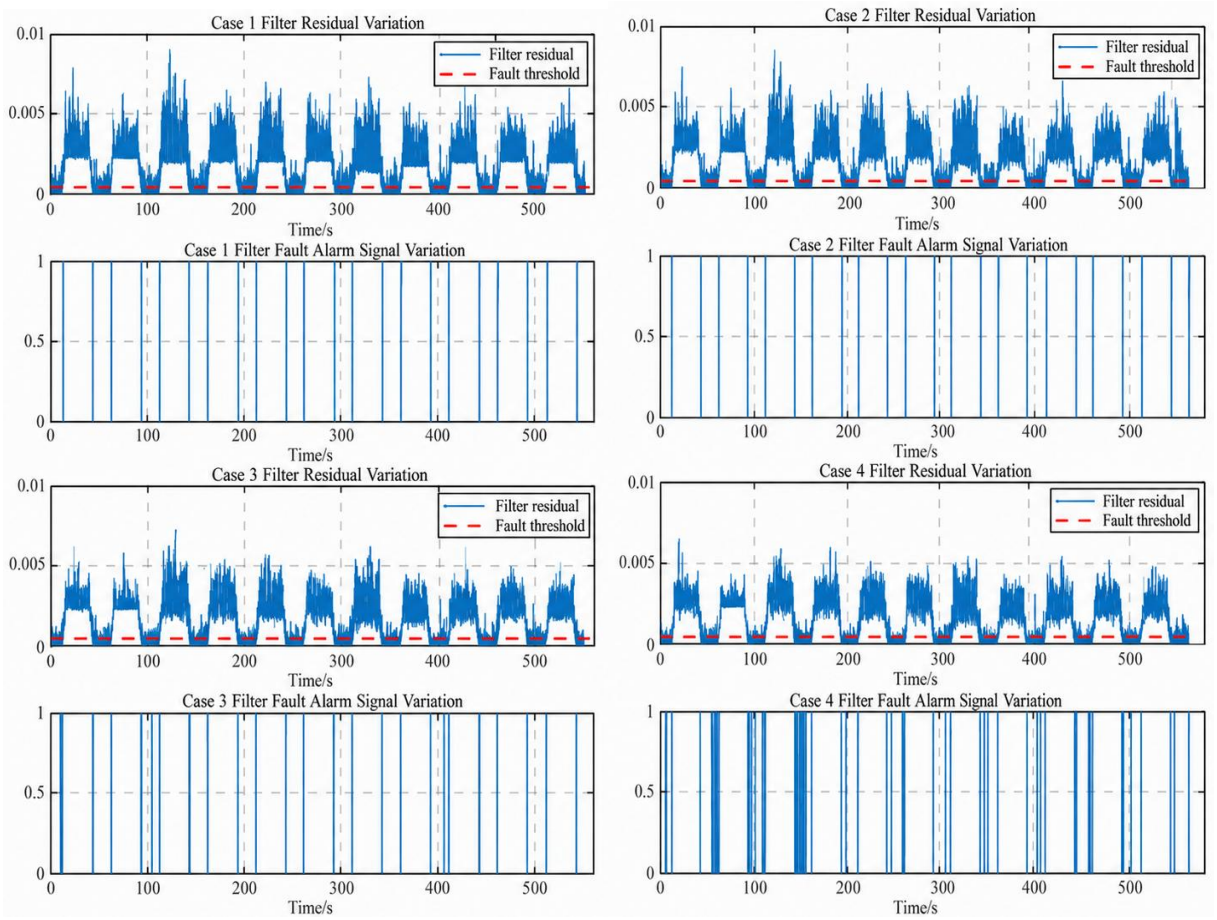


Figure 9 – Residuals and fault detection results under steady-state condition

As the packet loss rate increases from 0% to 75%, the fault detection rate rises from 99.06% to 99.66%, all exceeding 99%. At the same time, the false alarm rate increases from 1.58% to 6.83%,

which suggests that under severe packet loss conditions, a trade-off may need to be struck between fault sensitivity and the ability to correctly identify fault-free states.

Under dynamic conditions, the engine speed command varies continuously, and the combined influence of state evolution and network packet loss renders residual discrimination more challenging.

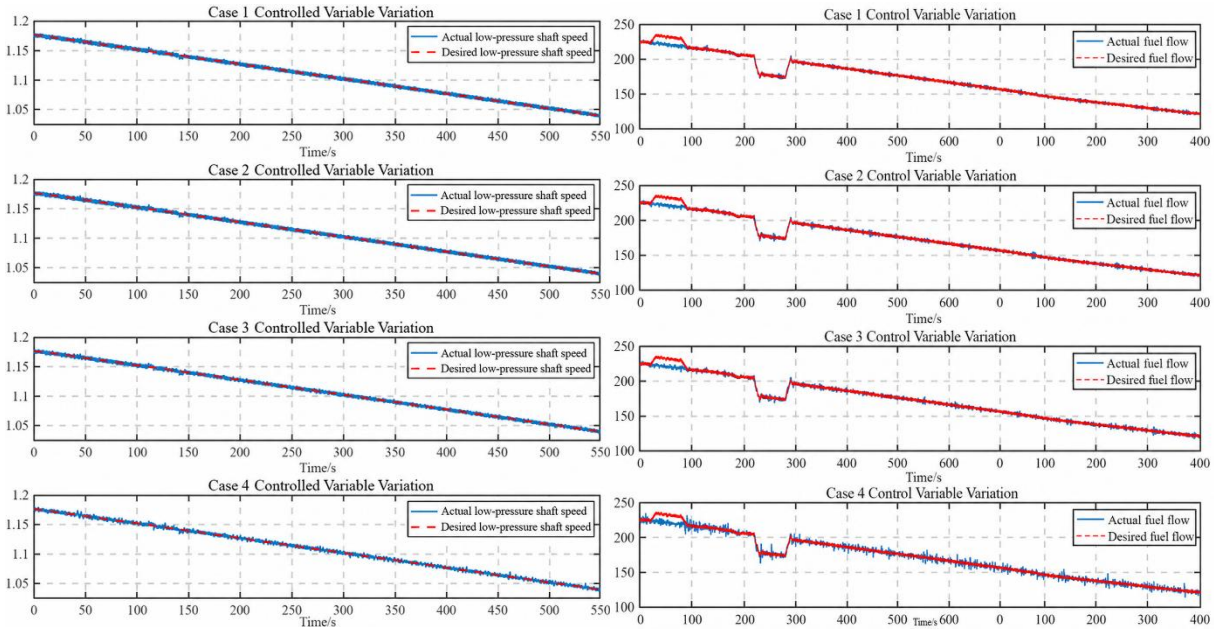


Figure 10 – Variations in controlled variable and control variable under dynamic-state condition

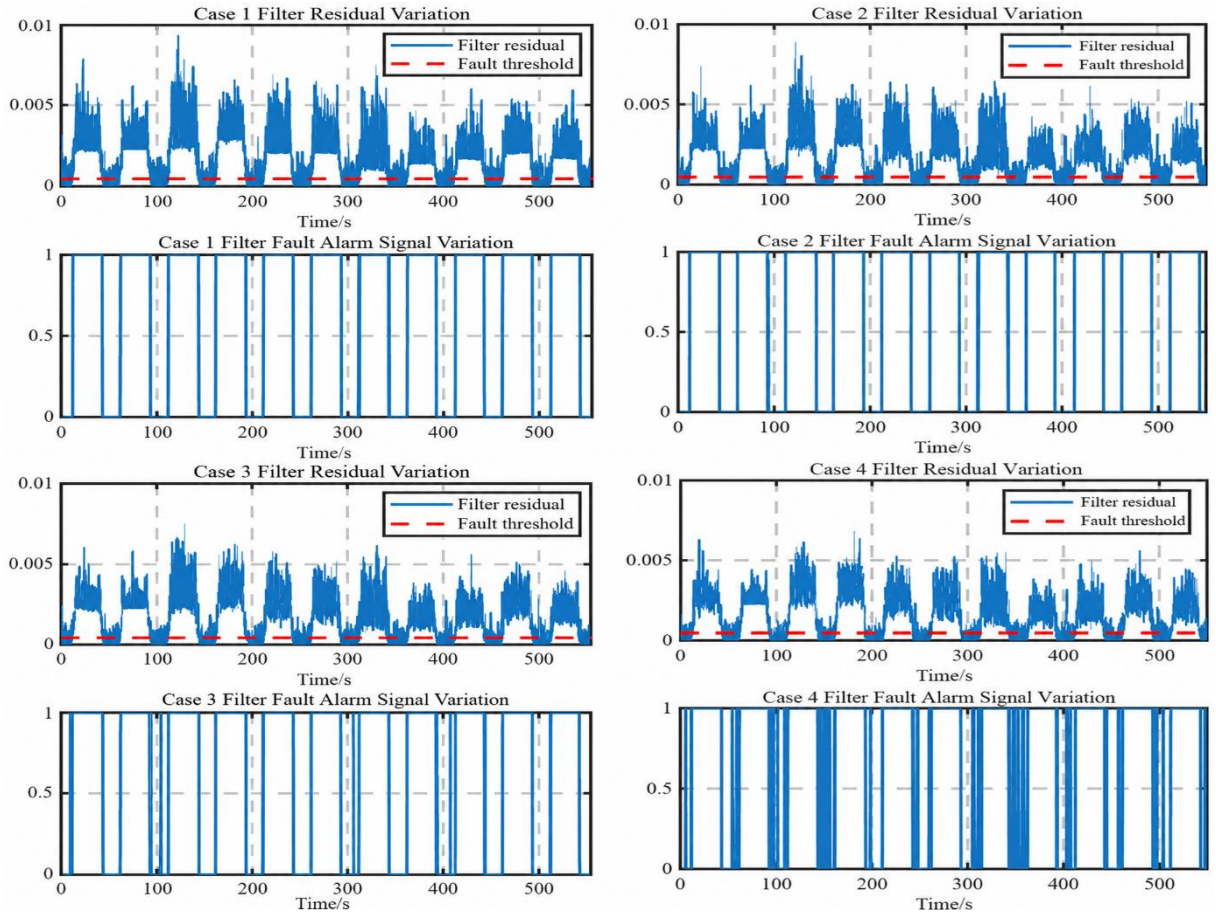


Figure 11 – Residuals and fault detection results under dynamic-state condition

The fault detection rates for Cases 1 to 4 are 98.91%, 99.28%, 99.37%, and 99.53%, respectively, all approaching or exceeding 99%. The missed detection rate decreases progressively from 1.09%

to 0.47%. These results indicate that the proposed method is capable of identifying fault characteristics with reasonable stability under dynamic operating conditions. Consistent with the steady-state findings, the false alarm rate increases with the packet loss rate, which implies that in practical applications the detection threshold may benefit from adjustment according to the mission phase and the acceptable risk profile.

Table 2 – Fault Detection Performance Under Different Packet Loss Rates

Case	Packet Loss Rate	Fault Detection Rate	False Alarm Rate
Steady-state	0%	99.06%	1.58%
	25%	99.54%	2.35%
	50%	99.64%	3.19%
	75%	99.66%	6.83%
Dynamic-state	0%	98.91%	1.96%
	25%	99.28%	2.48%
	50%	99.37%	3.40%
	75%	99.53%	7.04%

3.3 Node-Level Fault Isolation and Accommodation Results

The node-level fault isolation and Accommodation results are illustrated in Figures 12 and 13. The reduced-order filter bank demonstrates a high fault localization capability under both steady-state and dynamic conditions. Under steady-state conditions, the node fault isolation rate reaches 100% for Cases 1 and 2; at packet loss rates of 50% and 75%, the isolation rates are 99.98% and 99.77%, respectively, with only a small number of isolation failures observed. Under dynamic conditions, the isolation rate exhibits a slight decline as the packet loss rate increases; nevertheless, Case 4 still maintains 99.63%. These results indicate that the node-level diagnostic structure possesses a degree of robustness against communication packet loss.

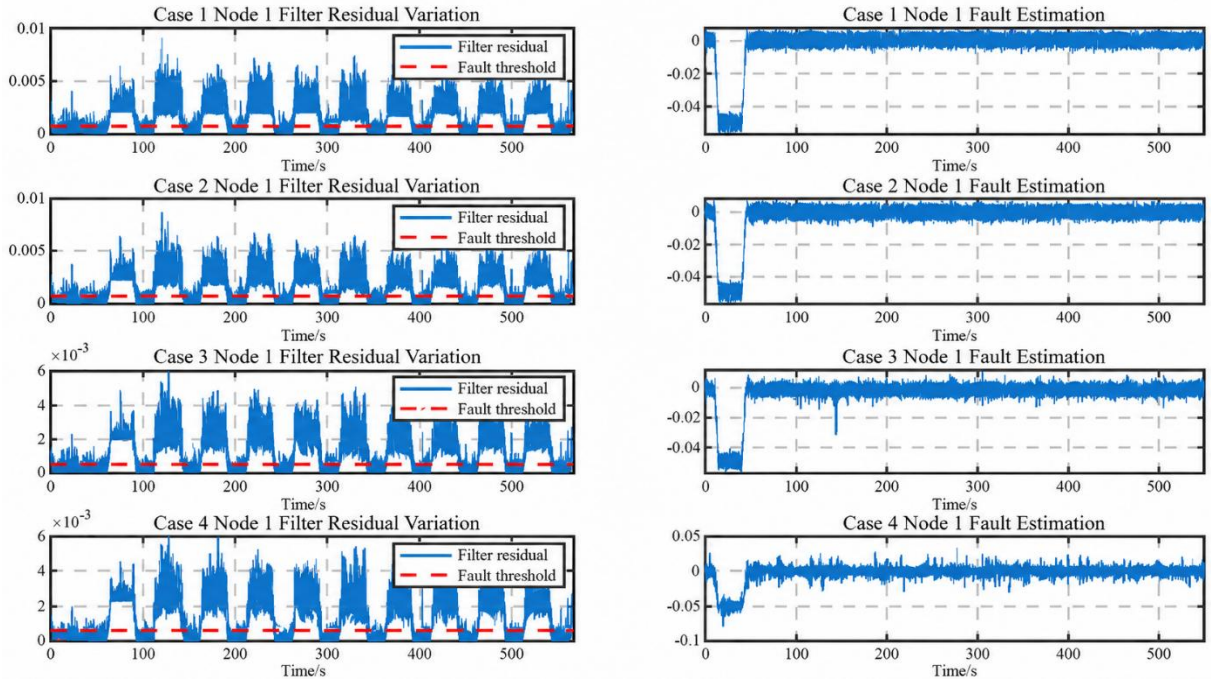


Figure 12 – Node-level fault isolation and estimation results under steady-state condition

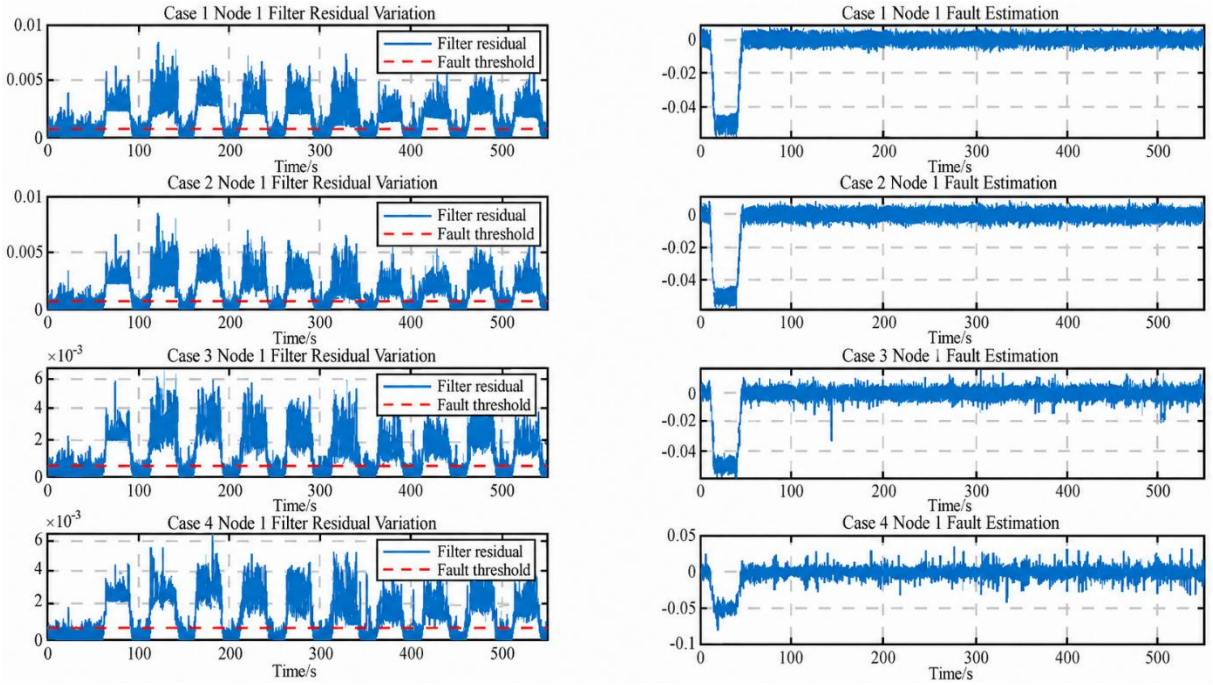


Figure 13 – Node-level fault isolation and estimation results under dynamic-state condition

With respect to fault estimation accuracy, the results across all operating conditions remain close to 99.4%. The steady-state Cases 1 to 4 yield 99.45%, 99.45%, 99.46%, and 99.41%, respectively; the dynamic Cases 1 to 4 yield 99.45%, 99.44%, 99.45%, and 99.37%. No marked degradation in estimation accuracy is observed as the packet loss rate increases, which suggests that the fault collapse coefficient and the reduced-order filter bank can effectively suppress cross-node fault coupling and maintain a stable estimate of node-level fault severity.

Table 3 – Node-Level Fault Isolation and Accommodation Performance

Case	Packet Loss Rate	Node Fault Isolation Rate	Fault Estimation Accuracy
Steady-state	0%	100.00%	99.45%
	25%	100.00%	99.45%
	50%	99.98%	99.46%
	75%	99.77%	99.41%
Dynamic-state	0%	100.00%	99.45%
	25%	99.95%	99.44%
	50%	99.88%	99.45%
	75%	99.63%	99.37%

4. Discussion

This paper has presented a robust fault diagnosis methodology for aero-engine networked distributed control systems operating under transmission uncertainties. By analysing the propagation mechanisms of sensor faults, actuator faults, and network-induced anomalies, a unified equivalent augmented fault-space model was constructed. This formulation enables control-system faults and network uncertainties to be represented within a single diagnostic framework, thereby avoiding the need for separate treatment of these two sources of disturbance.

To address the non-Gaussian noise characteristics arising from network delays and packet dropouts, an adaptive kernel-bandwidth minimum information entropy criterion was incorporated into the UKF framework, yielding the AMinIEC-UKF full-dimensional fault detector. Detection thresholds were derived using a measurement uncertainty quantification approach based on the chi-square distribution of the normalized weighted sum of squared residuals. The simulation results indicate that

the proposed method maintains a high fault detection rate under both steady-state and dynamic operating conditions, suggesting a satisfactory degree of adaptability to non-Gaussian residual disturbances.

To meet the requirements of distributed node-level diagnosis, a bank of reduced-order filters incorporating a fault collapse coefficient was developed, enabling simultaneous node-level fault isolation and fault severity estimation. The results obtained under a maximum packet loss rate of 75% demonstrate that the proposed method retains high fault detection rates, node isolation rates, and estimation accuracy, which indicates its potential utility for health management in aero-engine distributed control systems.

Several limitations of the present study should be acknowledged. The simulations reported here primarily consider one type of transmission uncertainty, namely packet dropouts. Additional network effects, including network delays, link jitter, clock drift, bandwidth contention, and concurrent multiple faults, warrant further investigation. Moreover, subsequent work could usefully employ hardware-in-the-loop or semi-physical test platforms to evaluate the real-time performance and reliability of the proposed algorithm under realistic communication links and onboard computational resource constraints. Such studies would represent an important step toward practical deployment.

5. Contact Author Email Address

Yuzhi Chen: yuzhi.chen@nwpu.edu.cn

6. Acknowledgments

The authors acknowledge the support from the National Natural Science Foundation of China (Grant No. 52402520).

7. Copyright Statement

The authors confirm that they, and/or their company or organization, hold copyright on all of the original material included in this paper. The authors also confirm that they have obtained permission, from the copyright holder of any third party material included in this paper, to publish it as part of their paper. The authors confirm that they give permission, or have obtained permission from the copyright holder of this paper, for the publication and distribution of this paper as part of the ICAS proceedings or as individual off-prints from the proceedings

References

[1] Lei B, Shen N, Ji D, Ouyang R, Yang L, Liu Q, Gao B, and Wang Z A Comprehensive Review of Key Technologies for Enhancing the Reliability of Aero-Engines, *IEEE Access*, Vol. 12, 2024, pp. 148315–148331.

[2] Litt JS Harnessing the Digital Transformation for Development of Electrified Aircraft Propulsion Control Systems, 2023-01–1510, October 2023.

[3] Liao Z, Wang J, Liu J, Geng J, Li M, Chen X, and Song Z Uncertainties in Gas-Path Diagnosis of Gas Turbines: Representation and Impact Analysis, *Aerospace Science and Technology*, Vol. 113, 2021, p. 106724.

[4] Liu X, Zhu J, Luo C, Xiong L, and Pan Q Aero-Engine Health Degradation Estimation Based on an Underdetermined Extended Kalman Filter and Convergence Proof, *ISA Transactions*, Vol. 125, 2022, pp. 528–538.

[5] Huang Y, Tao J, Sun G, Wu T, Yu L, and Zhao X A Novel Digital Twin Approach Based on Deep Multimodal Information Fusion for Aero-Engine Fault Diagnosis, *Energy*, Vol. 270, 2023, p. 126894.

[6] Liao Z, Zhan K, Zhao H, Deng Y, Geng J, Chen X, and Song Z Addressing Class-Imbalanced Learning in Real-Time Aero-Engine Gas-Path Fault Diagnosis via Feature Filtering and Mapping, *Reliability Engineering & System Safety*, Vol. 249, 2024, p. 110189.

[7] Li R, Nguang SK, Guo Y, and Chen Y Networked Control System Design for Turbofan Aeroengines with Aging and Deterioration, *Complexity*, Vol. 2018, No. 1, 2018, p. 6010216.

[8] Ge X, Yang F, and Han Q-L Distributed Networked Control Systems: A Brief Overview, *Information Sciences*, Vol. 380, 2017, pp. 117–131.

[9] Wang Y-A, Shen B, Zou L, and Han Q-L A Survey on Recent Advances in Distributed Filtering over Sensor Networks Subject to Communication Constraints, *International Journal of Network Dynamics and Intelligence*, Vol. 2, No. 2, 2023.

[10] Chen W, Hu J, Wu Z, and Ma S A Survey on Fault Detection for Networked Systems under Communication

Constraints, *Systems Science & Control Engineering*, Vol. 13, No. 1, 2025, p. 2460434.
[11] Xu Z, Ding B, and Zhang T Event-Based State and Fault Estimation for Stochastic Nonlinear System with Markov Packet Dropout, *Journal of the Franklin Institute*, Vol. 359, No. 2, 2022, pp. 1649–1666.
[12] El Abbadi R, and Jamouli H Fault Detection of a Networked Control System and Its Application to a DC Motor, *International Journal of Control, Automation and Systems*, Vol. 21, No. 6, 2023, pp. 1769–1779.
[13] Weiss M, Staudacher S, Mathes J, Becchio D, and Keller C Uncertainty Quantification for Full-Flight Data Based Engine Fault Detection with Neural Networks, *Machines*, Vol. 10, No. 10, 2022, p. 846.
[14] Wu J, Kong L, Kang S, Zuo H, Yang Y, and Cheng Z Aircraft Engine Fault Diagnosis Model Based on 1DCNN-BiLSTM with CBAM, *Sensors*, Vol. 24, No. 3, 2024, p. 780.
[15] Jung J-S, Son C, Rimell A, and Clarkson RJ A Framework for an ML-Based Predictive Turbofan Engine Health Model, *Aerospace*, Vol. 12, No. 8, 2025, p. 725.
[16] Ma Y, Zhu X, Lu J, Yang P, and Sun J Construction of Data-Driven Performance Digital Twin for a Real-World Gas Turbine Anomaly Detection Considering Uncertainty, *Sensors*, Vol. 23, No. 15, 2023, p. 6660.
[17] Chen B, Dang L, Gu Y, Zheng N, and Príncipe JC Minimum Error Entropy Kalman Filter, *IEEE Transactions on Systems, Man, and Cybernetics: Systems*, Vol. 51, No. 9, 2021, pp. 5819–5829.
[18] Dang L, Chen B, Huang Y, Zhang Y, and Zhao H Cubature Kalman Filter Under Minimum Error Entropy With Fiducial Points for INS/GPS Integration, *IEEE/CAA Journal of Automatica Sinica*, Vol. 9, No. 3, 2022, pp. 450–465.
[19] He J, Wang G, Yu H, Liu J, and Peng B Generalized Minimum Error Entropy Kalman Filter for Non-Gaussian Noise, *ISA Transactions*, Vol. 136, 2023, pp. 663–675.
[20] Wang G, Chen B, Yang X, Peng B, and Feng Z Numerically Stable Minimum Error Entropy Kalman Filter, *Signal Processing*, Vol. 181, 2021, p. 107914.